Source Rupture Process of the Tecomán, Colima, Mexico Earthquake of 22 January 2003, Determined by Joint Inversion of Teleseismic Body-Wave and Near-Source Data

AUTHOR(S):

Yagi, Yuji; Mikumo, Takeshi; Pacheco, Javier; Reyes, Gabriel

Bulletin of the Seismological Society of America, Vol. 94, No. 5, pp. 1795–1807, October 2004

Source Rupture Process of the Tecomán, Colima, Mexico Earthquake of 22 January 2003, Determined by Joint Inversion of Teleseismic Body-Wave and Near-Source Data

by Yuji Yagi, Takeshi Mikumo, Javier Pacheco, and Gabriel Reyes

Abstract The spatial and temporal slip distribution of the Tecomán, Colima, Mexico earthquake is estimated from near-source strong-motion and teleseismic body-wave data. To perform a stable inversion, we applied smoothing constraints and determined their optimal relative weights on the observed data using an optimized Akaike's Bayesian information criterion (ABIC). The source parameters are as follows: (strike, dip, slip) = (300°, 20°, 93°), seismic moment $M_0 = 2.3 \times 10^{20}$ N m; source duration = 30 sec; along-strike distance = 35 km; along-dip distance = 70 km. We found that the rupture process can be divided into three stages: the rupture nucleated near the hypocenter (stage I), then it broke the first asperity centering about 15 km southwest from the epicenter (stage II); and the rupture propagated to the northeast and the second asperity was broken (stage III). We also estimated the shear-stress change due to the rupture process of the mainshock on and around the major fault zone. It appears that one cluster of aftershocks for the first 5 days, which took place in and adjacent to the zones of stress, increased due to the fault rupture during the mainshock, but overall correlation between the aftershock location and the stress pattern is not clear.

Introduction

On 22 January 2003, a powerful earthquake struck part of southern and central Mexico, killing at least 21 people and causing serious damage, mainly in the state of Colima. The earthquake information initially provided by the U.S. Geological Survey is as follows: origin time = 22 January 2003 02h06m35sec (UT); epicenter = 18.807° N, 103.886° W; depth = 30 km; moment magnitude = 7.8. In this region, the oceanic Rivera (RIVE) and Cocos (COCOS) plates subduct beneath Mexico, which forms part of the continental North American (NOAM) plate, where four great earthquakes occurred on 3 June 1932 (M_s 8.1), 18 June 1932 (M_s 7.8), 30 January 1973 (M_s 7.5), and 10 October 1995 (M_s 7.3; M_w 8.0). The tectonic settings and aftershock areas of these great earthquakes are shown in Figure 1.

The 2003 Tecomán, Mexico earthquake occurred near a diffuse-triple junction, and the boundary between the RIVE and COCOS plates is uncertain (e.g., Bandy *et al.*, 1995; DeMets and Wilson, 1996). The convergence rate between the RIVE-NOAM and COCOS-NOAM near the junction is roughly equal to 5 cm/yr (DeMets and Stein, 1990; Bandy *et al.*, 1995). To gain an understanding of the seismotectonics of this region, it is important to investigate the coseismic slip area of these great earthquakes.

In general, the teleseismic body waves contain the information on the overall moment release rate and the depth range of the rupture area, whereas the near-source waveforms contain most of the information on the detailed slip process in the source area. Therefore, to estimate the detailed and stable source process, it is important to use both the teleseismic body-wave and near-source data.

In this study, we constructed a detailed source model of this earthquake, using the near-source records obtained by the Universidad Nacional Autonoma de Mexico (UNAM) plus the teleseismic data collected by the Data Management Center of the Incorporated Research Institutions for Seismology (IRIS-DMC). We also compared stress change due to the coseismic slip with aftershock distribution.

Data

We retrieved teleseismic body-wave (*P* and *SH* waves) data recorded at IRIS-DMC stations via the Internet. Fourteen components at 12 stations were selected from the viewpoint of good azimuthal coverage. The locations of seismograph stations are shown in Figure 2. The teleseismic body waves were windowed for 60 sec, starting 10 sec before the origin time, bandpassed between 0.01 and 2.0 Hz, and then converted into ground velocity with a sampling time of 0.25 sec.

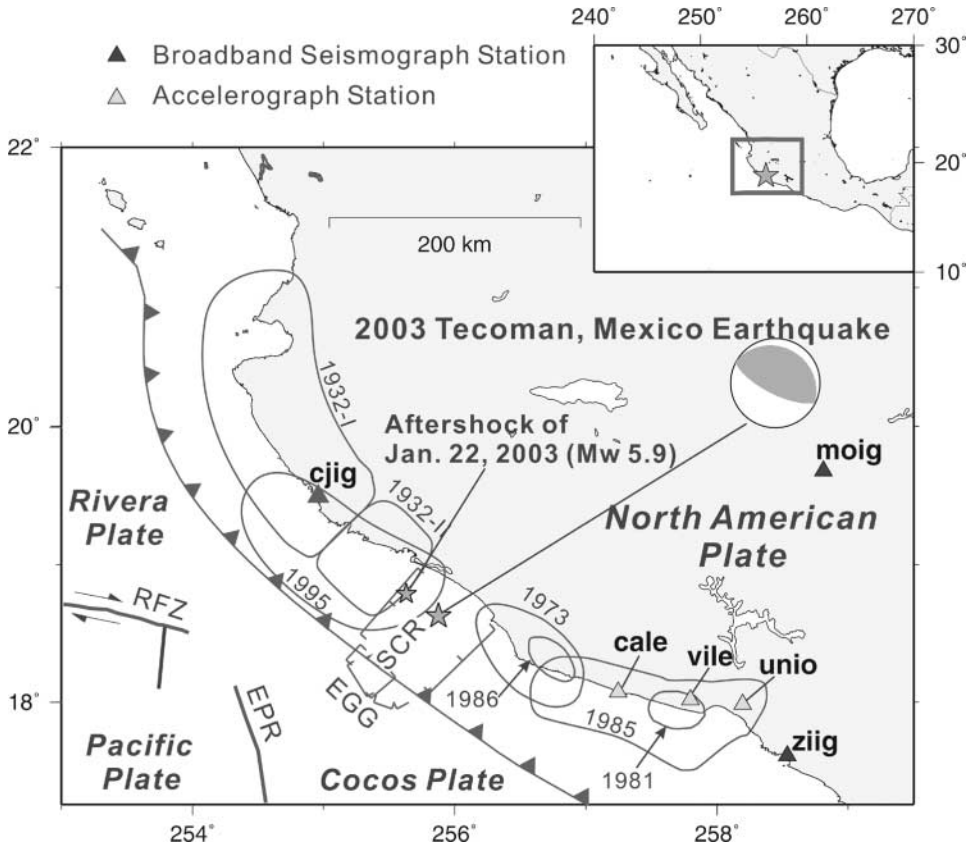

Figure 1. Geographic map showing the epicentral location (star) of the 2003 Tecomán, Colima, Mexico earthquake. RFZ, Rivera Fracture Zone; EPR, East Pacific Rise; EGG, El Gordo Graben; SRC, Southern Colima Rift. The contours show the aftershock area of large/great earthquakes in the region (modified from Singh *et al.*, 2003). The black triangles and gray triangles indicate broadband seismograph stations and accelerograph stations, respectively. The focal mechanism was determined by our study.

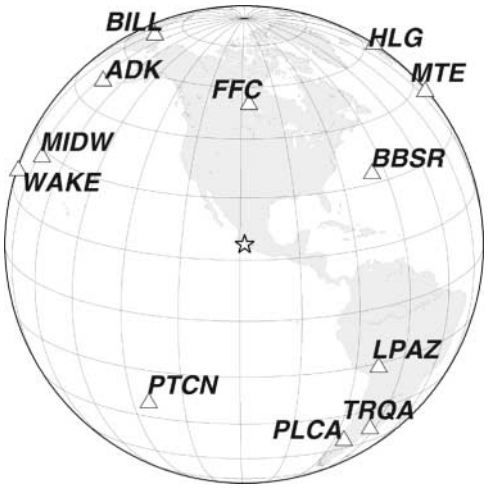

Figure 2. Teleseismic station map shown as a map view. The star represents the epicenter of the mainshock.

We also used 18 components of strong-motion data obtained from three broadband seismograph stations of the Servicio Sismologico Nacional (SSN), UNAM, and three accelerograph stations of Instituto de Ingenieria, UNAM. The locations of these near-source stations are shown in Figure 1. The acceleration data were bandpassed between 0.01 and 0.5 Hz and numerically integrated to ground velocity with a sampling time of 0.25 sec; and the broadband velocity data were bandpassed between 0.01 and 0.5 Hz with a sampling time of 0.25 sec. Because the start time of near-source strong motion is not accurate, we made time corrections so that the observed *P*-wave arrivals coincide with the theoretical arrival time of *P* waves.

The broadband velocity seismogram recorded at the station cjig and its waveform amplified 100 times are shown in Figure 3. It is possible to identify small-amplitude motions lasting for 4 sec before a large-amplitude phase. Since this small phase is too diminutive to identify on teleseismic body waveforms, it was difficult to detect the first motion of the *P* wave at teleseismic seismograph stations. To correct the timing, we performed preliminary waveform inversion using

the near-source data set and calculated a synthetic waveform for each teleseismic station. Later, we estimated timing corrections where the correlation coefficient between the observed and synthetic waveforms takes the maximum value.

Waveform Inversion

To construct the source model in an objective fashion, we developed a numerical method for the standard waveform inversion scheme (e.g., Harzell and Heaton, 1993; Yoshida, 1992). Following the formulation of Yoshida (1992), we represented the rupture process as a spatiotemporal slip distribution on a fault plane. First, we divided the fault plane into $M \times N$ subfaults with length dx and width dy. Next, we described the slip-rate function on each subfault with linear B splines that are a series of L triangle functions with rise time τ. Finally, we described the fault-slip vector with K basis slip vectors. Using this source model, the observed seismic waveform at the station j is expressed by

$$W_j^{\mathrm{obs}}(t_i) = \sum_{mnlk} X_{mnlk} g_{mnkj} (t_i - (l-1)\tau - T_{mn}) + e_j, \quad (1)$$

where X_{mnkl} is the kth component of slip at the mnth subfault at the lth timestep; $g_{mnkj}(t)$ is the Green's function (elementary wave from a point source at the mn subfault with unit slip); T_{mn} is the start time of the basis function at each subfault; e_j is assumed to be the Gaussian error with variance of σ_j. We calculated the Green's functions for teleseismic body waves using the method of Kikuchi and Kanamori (1991). Green's functions for near-source ground motion were calculated by the discrete wavenumber method developed by Kohketsu (1985). The source-region structure models used to compute both the teleseismic body waves and near-source ground motion are given in Table 1. To explain the observed waveform of aftershocks, we modified the structure model given in Pacheco *et al.* (1997). Figure 4 shows the theoretical displacement waveforms from a point source and the observed waveforms for the aftershock of 22 January 2003 (M_w 5.9). The location of this aftershock is shown in Figure 1. Because we assumed simple source-time function, we can not reconstruct the high-frequency component of the observed waveform. However, the general feature of the observed waveforms can be explained by using our structure model. We have also added 1-km-thick layer for teleseismic body waves to model complicated water reverberations. In the present case, considering the quality of the observed records, we took σ_j in the near-source and far-field P waves and SH waves as 20%, 10%, and 20% of their maximun amplitude, respectively.

The observation equation of (1) can be rewritten in vector form as

$$\mathbf{Y_j} = \mathbf{A_j x} + \mathbf{e_j}, \quad (2)$$

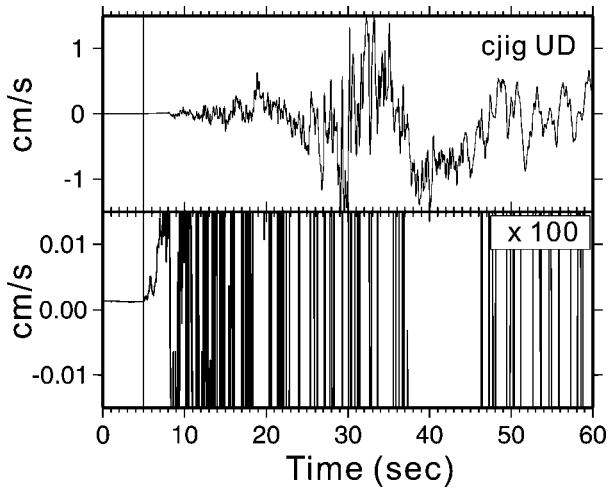

Figure 3. Seismograms recorded at cjig station. The top trace is the vertical component of the velocity waveform, and the bottom trace is amplified 100 times.

Table 1
Structure

V_p (km/sec)	V_s (km/sec)	Density (10^3 kg/m^3)	Q_p	Q_s	Thickness (km)
For teleseismic body wave					
1.5	0	1.0			1.0
5.54	3.20	2.50			3.0
5.69	3.29	2.70			5.0
6.27	3.62	2.80			9.7
6.71	3.87	2.90			17.3
8.10	4.68	3.30			—
For strong ground motion					
5.54	3.20	2.50	300	150	4.0
5.69	3.29	2.70	500	250	5.0
6.27	3.62	2.80	600	300	9.7
6.71	3.87	2.90	800	400	17.3
8.10	4.68	3.30	1200	600	—

where $\mathbf{A_j}$ is a matrix of n_j (number of data points at station j) $\times$ N_a (number of model parameters) dimension. In general, an increase in the number of model parameters may give rise to instability in the solution with the result that even a small change in the data will result in a large change in the solution. To obtain more stable results, we applied smoothing constraints to the slip distribution with respect to time and space. The smoothness constraint with respect to time is:

$$0 = X_{mnk(l-1)} - 2X_{mnkl} + X_{mnk(l+1)} + e_t, \quad X_{mnko} = X_{mnkl} = 0, \quad (3)$$

where e_t is the Gaussian error. This can be rewritten in the following simple vector form:

$$\mathbf{0} = \mathbf{Tx} + \mathbf{e_t}, \quad (4)$$

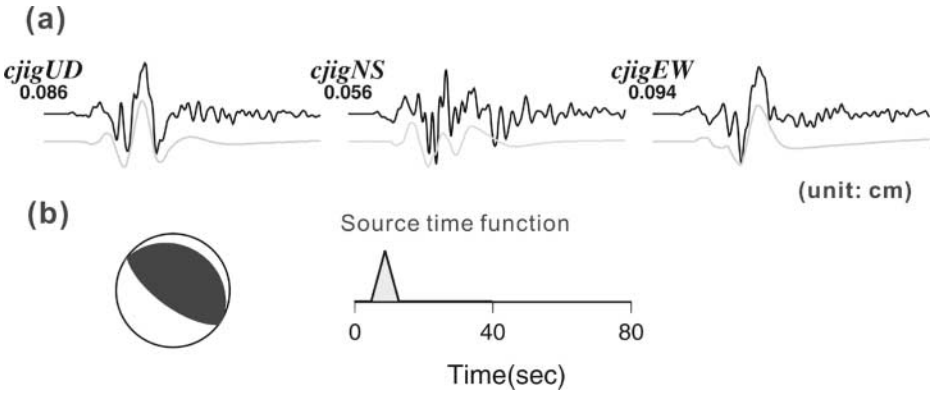

Figure 4. (a) Theoretical waveforms (gray curves) from a point source and observed waveforms (black curves) for the aftershock of 22 January 2003 (M_w 5.9). The numbers below the station code indicate the maximum amplitude. (b) Assumed source-time function and focal mechanism.

where $\mathbf{T}$ is $N_l \times N_a$ matrix ($N_l = MNLK$). The smoothness constraint on the spatial distribution of total slip is introduced by a Laplacian finite-difference operator:

$$0 = \sum_l X_{(m-1)nkl} + X_{(m+1)nkl} + X_{m(n-1)kl} + X_{m(n+1)kl} - 4\,X_{mnkl} + e_d \qquad (5)$$
$$X_{0nkl} = X_{m0kl} = X_{(M+1)nkl} = X_{m(N+1)kl} = 0.$$

This can be rewritten in the following simple vector form:

$$\mathbf{0} = \mathbf{Dx} + \mathbf{e_d}, \qquad (6)$$

where $\mathbf{D}$ is $N_2 \times N_a$ matrix ($N_2 = MNK$).

For the analysis of seismic waves, using the observed data with two constraints, we determine the model parameters that minimize the sum of squared residuals, S, given by

$$S(\mathbf{x}, \sigma_j, \sigma_t, \sigma_d) = \sum_j \frac{1}{\sigma_j^2} \|\mathbf{y}_j - \mathbf{A}_j\,\mathbf{x}\|^2 + \frac{1}{\sigma_t^2}\|\mathbf{Tx}\|^2 + \frac{1}{\sigma_d^2}\|\mathbf{Dx}\|^2, \qquad (7)$$

For given values of σs, we can determine the best estimates of model parameters using the least-squares method discribed by Jackson and Matsu'ura (1985). The values of σ_t and σ_d cannot be estimated directly, but σ_j can be estimated by the quality of data. To determine σ_t and σ_d objectively, we adopted the minimum Akaike's Bayesian information criterion (ABIC) (Akaike, 1980). The optimal ABIC formulation of two types for partially dependent prior information was developed by Fukahata *et al.* (2003, 2004), and its validity has already been checked. The optimal ABIC for the present case is expressed using the following equation:

$$\text{ABIC}(\mathbf{x}, \sigma_t, \sigma_d) = N \log S(\mathbf{x}, \sigma_j, \sigma_t, \sigma_d) - \log\left\|\frac{1}{\sigma_t^2}\mathbf{T}^t\mathbf{T} + \frac{1}{\sigma_d^2}\mathbf{D}^t\mathbf{D}\right\| + \log\left\|\sum_j \frac{1}{\sigma_j^2}\mathbf{A}_j^t\mathbf{A}_j + \frac{1}{\sigma_t^2}\mathbf{T}^t\mathbf{T} - \frac{1}{\sigma_d^2}\mathbf{D}^t\mathbf{D}\right\| + C. \qquad (8)$$

N is the total number of the observation equations. We apply a grid-search method to obtain optimal values of σ_t and σ_d. In this article, to solve the least-squares problem with a positivity constraint on the model parameters, we used the nonnegative least-squares (NNLS) algorithm of Lawson and Hanson (1974).

Fault Model

We assumed that faulting occurs on a single fault plane and that the slip angle remains unchanged during the rupture. We adopted the fault mechanism of (strike, dip, slip) = (300°, 22°, 93°), and the epicenter determined by Colima University (latitude = 18.71° N; longitude = 104.13° W). This fault mechanism is modified slightly from the Harvard CMT solution to be consistent with the amplitude of *P* waves and with the geometry of the plate boundary that has been determined by the focal mechanism and seismicity (Pardo and Suárz, 1995). Figure 5 shows theoretical teleseismic waveforms from a point source for different source depths and the observed waveforms. The shape of the theoretical waveforms vary with depth due to varying the timing of the reflected phases (e.g., *pP* and *sP*). The shape of the observed waveforms is similar to the theoretical waveforms for a depth of 20 km. This implies that the depth of major moment release is located near 20 km.

To obtain gross features and some details of the rupture process, we divided the procedure into two steps. In the first step, we took a broad fault area of 100 × 90 km to obtain a rough estimate of the rupture area, which we divided into

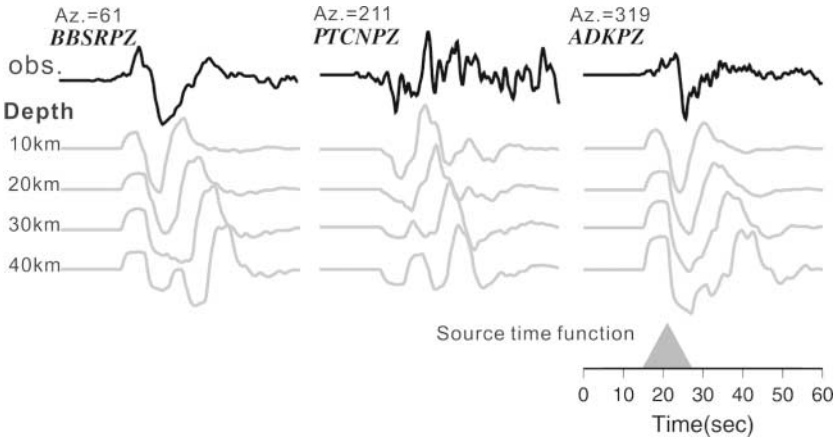

Figure 5. Theoretical waveforms (gray curves) at different source depths and observed waveforms (black curves).

10 × 9 subfaults, each with an area of 10 × 10 km. If the start time of the basis function at each subfault T_{mn} of equation (1) is set to 0 sec, we can allow all subfaults to slip at any time. Although this model is flexible, the computation time is long. To save the computation time, we assume a first rupture front velocity V_i, which gives the start time of the basis function at each subfault T_{mn} of equation (1). For V_i, we tested a range of values between 2.5 and 4.5 km/sec, and finally found that a velocity of 3.5 km/sec shows a minimum variance. This is close to the shear-wave velocity in the source region. The slip-rate function on each subfault is expanded into a series of eight triangle functions with a rise time of 2 sec. Because the hypocentral depth is not adequately constrained by the local seismological network, we varied the hypocentral depth from 10 to 35 km in increments with 2.5 km in the inversion procedure with the fault mechanism and epicenter fixed and found its minimum variance at 20 km (Fig. 6). Through the inversion procedure, the effective rupture area was estimated to be 40 × 70 km.

In the second step, the fault plane was confined to a narrower area of 70 × 85 km and divided into 14 × 17 subfaults, each having an area of 5 × 5 km. The slip-rate function on each subfault is expanded into a series of 13 triangle functions with a rise time of 1 sec. The rupture front velocity is also set at 3.5 km/sec in this case.

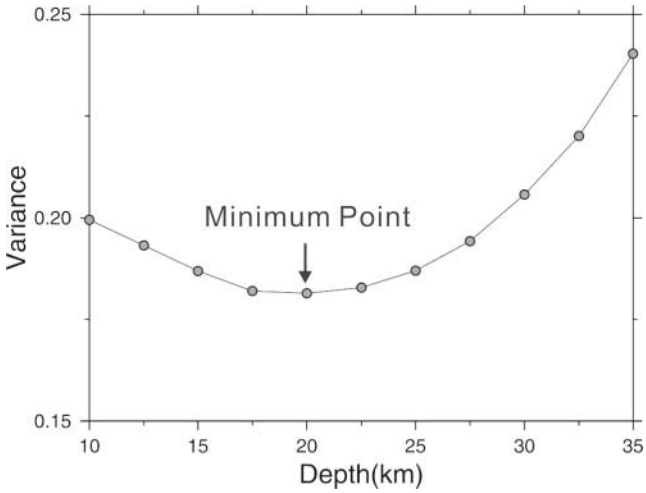

Figure 6. Waveform variance determined from the preliminary analysis plotted as a function of hypocentral depth. The differences from the minimum (depth = 20.0 km) are shown.

Source-Rupture Process

The inversion results are shown in Figures 7, 8, and 9. Figure 7 shows the final dislocation on the fault plane, and Figure 8a depicts its distribution on the map. Figure 9 represents a snapshot of the slip rate at every 2 sec. The source-rupture process obtained may be divided into three stages from I to III. At stage I, the rupture nucleated near the hypocenter during the initial stage of 4 sec. The seismic moment at this stage is 2.5 × 10^{18} N m (M_w 6.2), which is significantly smaller than the total seismic moment. At stage II, the rupture propagated to the southwest and broke the first asperity (A) centered at about 15 km southwest from the epicenter during 4 to 10 sec after the initial break. The seismic moment at this stage is 2.5 × 10^{19} N m (M_w 6.9). At stage III, the rupture propagated to the northeast and broke asperity (B) centered at about 25 km northeast from the epicenter.

Figure 8b shows the slip function inferred for subfaults near the asperities. The mean source-time function at asperities A and B lasts about 7 and 6 sec, respectively. The source-time function consists of the dislocation rise time and the rupture propagation time over the subfaults. In the present case the rupture propagation time is about 2 sec. Accordingly, the mean rise times at A and B are about 5 and 4 sec, respectively. Although its difference is quite small, the slightly longer rise time on asperity A at shallower depths appears consistent with the general trend of source durations for shallow subduction earthquakes, which might be attributed to variable frictional properties or lower strength of the plate interface at shallower depths (Bilek and Lay, 2002).

The maximum slip amounts to 3.4 m at about 15 km southwest of the epicenter. Total seismic moment is M_o =

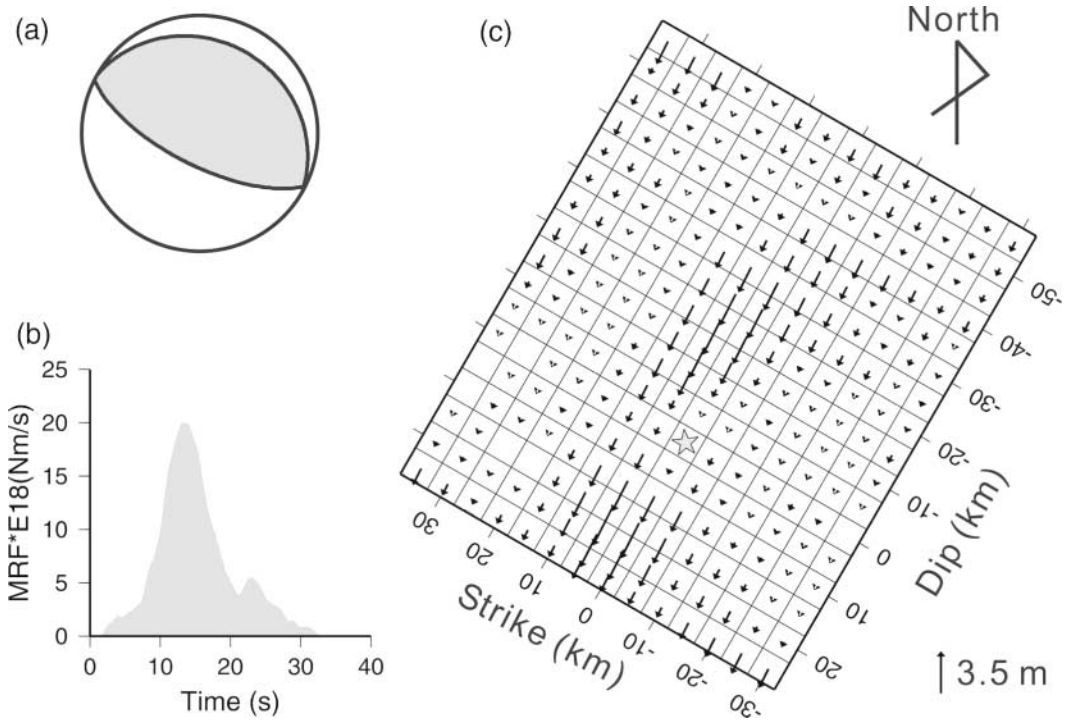

Figure 7. Final results of our joint inversion. (a) Focal mechanism. (b) Total moment-rate function. (c) Distribution of coseismic slip vectors. The star indicates the location of the initial break.

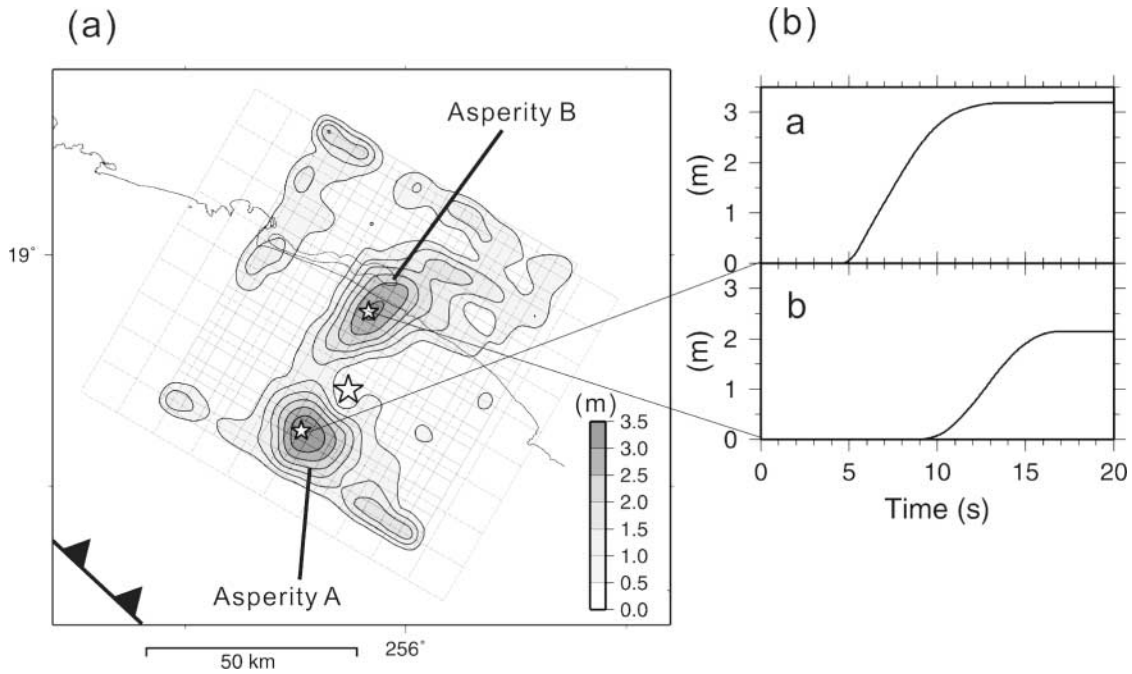

Figure 8. (a) Distribution of coseismic slip on the map. The star indicates the location of the initial break. (b) Slip functions obtained in this study for subfaults A and B shown in Figure 6.

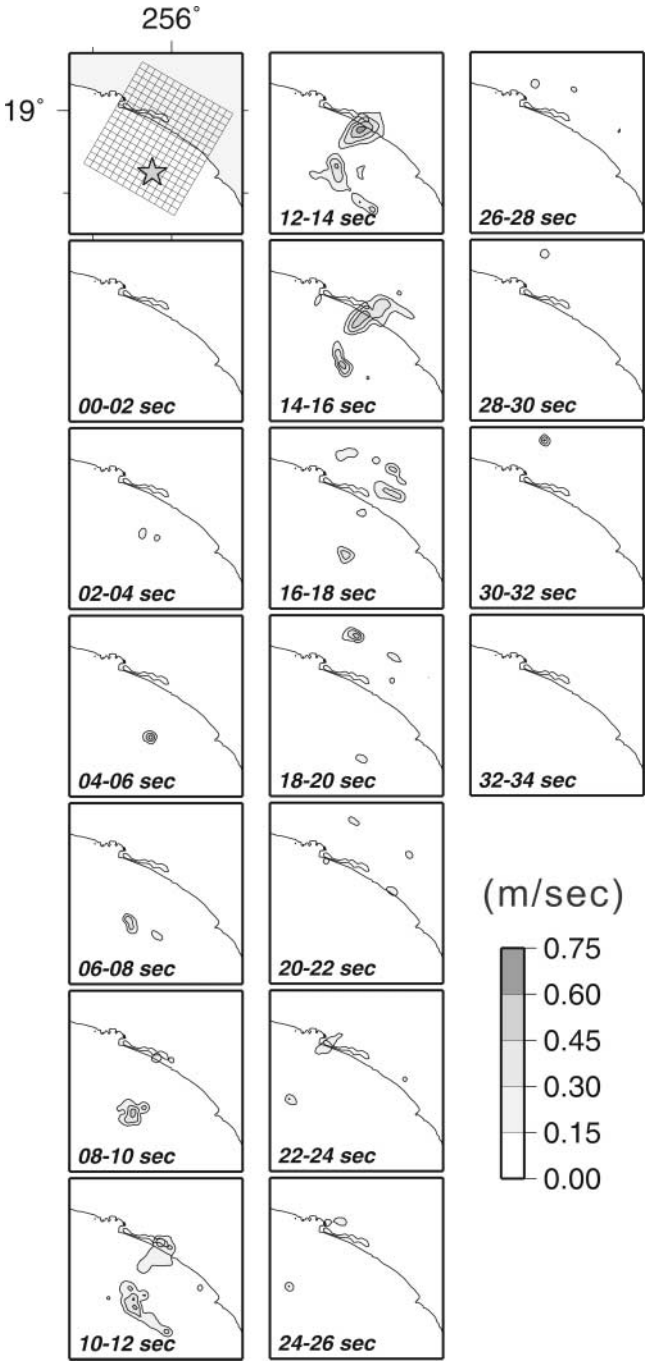

Figure 9. Snapshots of the surface projection of the slip rates at every 2 sec. The star indicates the epicenter of the 2003 Tecomán, Mexico earthquake.

2.3×10^{20} N m ($M_w = 7.5$), which is in agreement with that of the Harvard CMT, 1.62×10^{20} N m. The total source duration is about 30 sec. The rupture propagates mainly along the dip direction, and the along-strike length of the rupture area is significantly shorter than its down-dip width. The rupture area appears to extend parallel to the transition zone between the RIVE and COCOS plates. It should be noted that the hypocenter is located near a narrow part of the slip area, where the amount of slip is very small.

Figure 10 displays a comparison between the observed records (black) and the synthetics (gray). The waveform match is very good except for the MOIG station located 329 km northeast of the hypocenter. The discrepancy for this station may come from the assumed structure, which is not suitable for the station.

In the present analysis, the near-source data are very limited in azimuthal coverage. Stations CALE, VILE, UNIO, and ZIIG are nearly in the same azimuth; the waveform observed at MOIG cannot be constructed by our source model, so effectively there are two azimuths represented. Although this is not a good data set when compared with most strong-motion inversions, our result seems to have a good resolution. This result may come from the advantage of the joint inversion of teleseismic body-wave and strong-motion data with an optimized ABIC. Fukahata *et al.* (2003a,b) show that the optimized ABIC is particularly useful even with the insufficient observed data set.

We checked the resolution of our source model using a synthetic test. We generated the synthetic data corresponding to the actual station distribution using an assumed source model, which corresponds to a smoothed model of the main part of Figure 8a. A random Gaussian noise having a standard deviation of 5% of the maximum amplitude was added to each synthetic data. We tried to invert the source model for three different data sets: both of the teleseismic body-wave and near-source data, only the teleseismic body wave, and only the near-source data. The source models obtained from each data set are shown in Figure 11. From this figure, we can see that the slip patterns inverted from each data set are well reproduced. The slip distribution inverted both from the teleseismic body-wave and near-source data is almost same as the assumed slip distribution, whereas the slip models inverted only from the teleseismic body-wave or near-source data are simplified in the comparison with the assumed slip distribution. This result shows that the resolving power either of the teleseismic or near-source data sets is insufficient to reconstruct the assumed source model but that of both the teleseismic and near-source data is enough to reconstruct the assumed source model.

As shown previously, the slip distribution of the 2003 Tecomán earthquake extended to the northeast direction. The rupture pattern should affect the distribution of seismic intensity. Singh *et al.* (2003) obtained an isoseismal map based on reports mainly from local government agencies and from field inspection teams. Their results show that a large ground-motion area with VIII on the modified Mercalli intensity scale extended to the northeast, which is consistent with that expected from our source model.

Coseismic Stress Change and Aftershock Distribution

We also estimate the coseismic change of shear stress on and around the dipping fault plane due to the rupture process of the mainshock to compare it with aftershock distribution. Calculations of the shear-stress change is based on

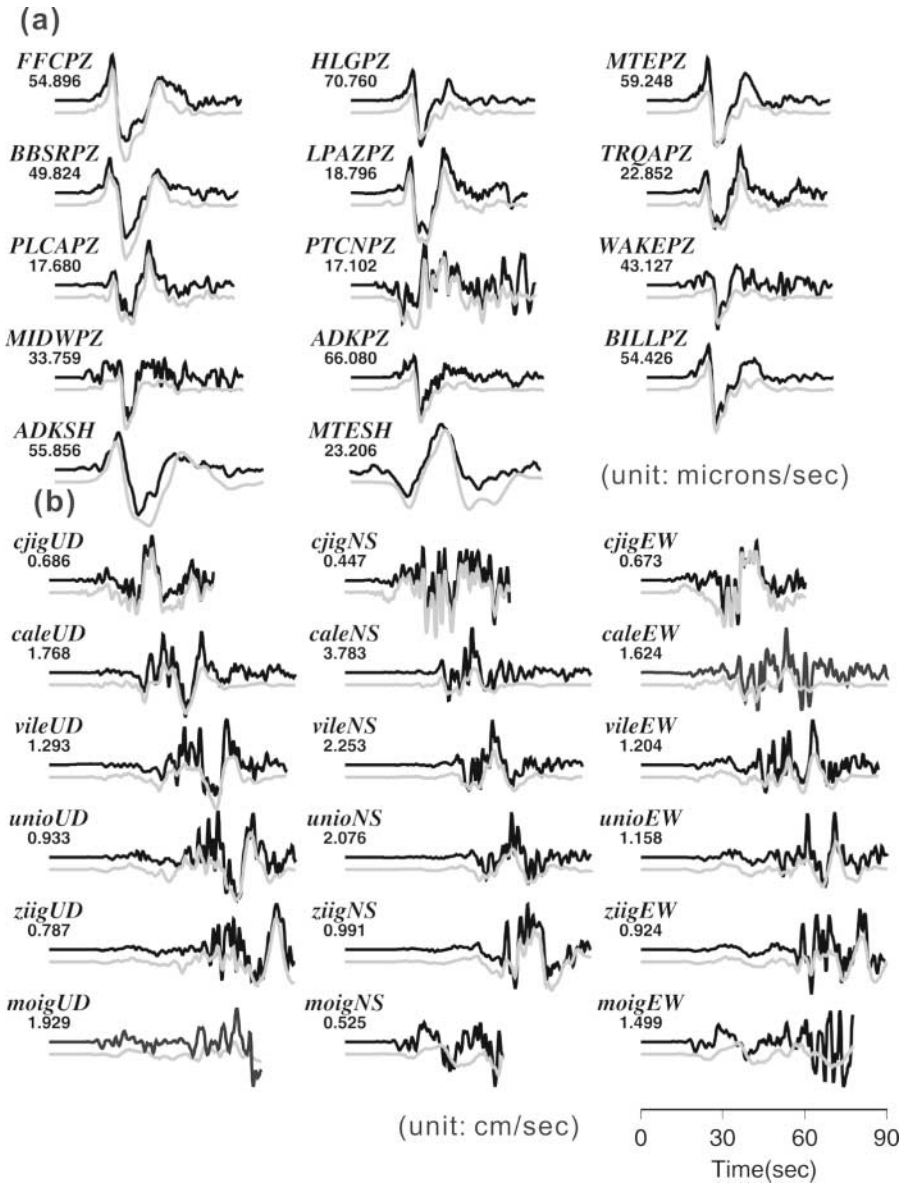

Figure 10. Comparison of the observed waveforms (upper trace) with the calculated waveforms (lower trace). The numbers below the station code indicate the maximum amplitude. (a) Teleseismic body wave. (b) Strong motion data.

the slip distribution (Fig. 5) obtained from the afore described waveform inversion. The method used here is from formulations for static dislocation in a 3D homogeneous half-space (Okada, 1992), incorporating elastic parameters in the third layer given in Table 1. We calculate the change of the shear-stress component parallel to the slip direction on the mainshock fault plane. This is because the two largest aftershocks that occurred in the west of the mainshock epicenter had nearly the same focal mechanism as that of the mainshock (Singh *et al.*, 2003), although the mechanism of other minor aftershocks is not well known.

Figure 12 shows the static shear-stress change thus calculated. Because the slip distribution obtained from the kinematic waveform inversion has somewhat larger estimation errors near the fault edges, we are mainly interested in the stress change in the central part of the fault to see whether there is any possible correlation with aftershock distribution. It is found that the maximum stress drop in a zone of a large slip of 3.1 m northeast of the epicenter is about 9.4 MPa (asperity B), and the maximum stress drop in a zone of large slip of 3.4 m is about 10.7 MPa (asperity A). On the other hand, we notice a zone of stress increase up to 4.5 MPa trending in the northwest–southeast direction just northeast of the epicenter, and another zone of stress increase of 4.0 MPa west of the large stress drop zone (asperity B). Additional dynamic rupture calculations, including a horizontally layered structure (Mikumo and Miyatake, 1993; Mikumo *et al.*, 2002), which have been made to check the possibility of

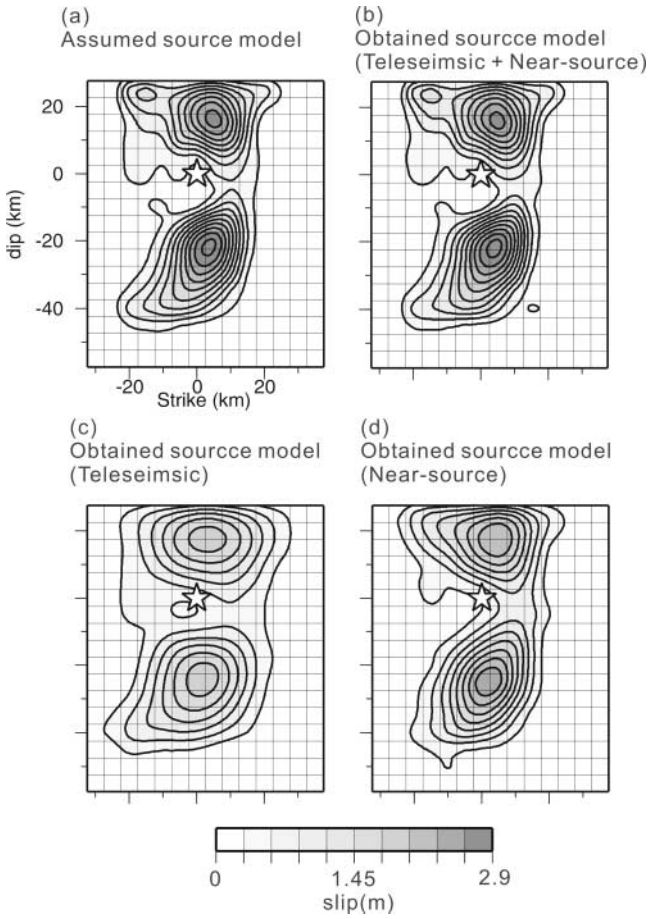

Figure 11. Results of the synthetic test. (a) Slip distribution of assumed source model. (b) Slip distribution obtained from both the teleseismic body-wave and the near-source data. (c) Slip distribution obtained from the teleseismic body wave. (d) Slip distribution obtained from the near-source data.

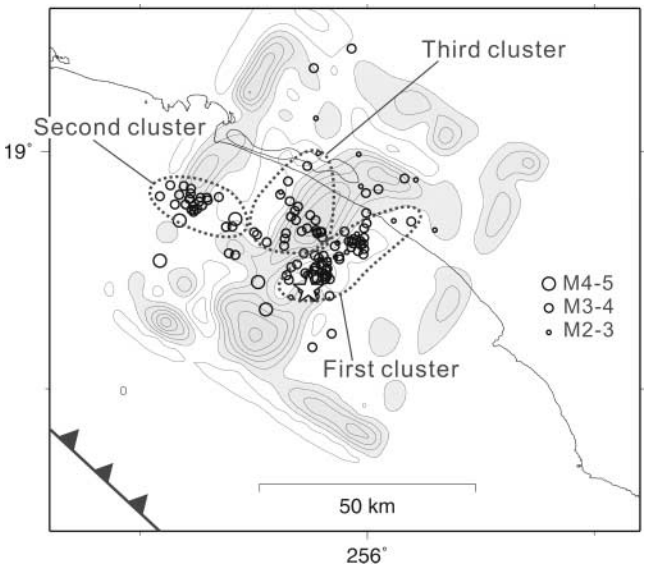

Figure 12. Distribution of coseismic stress change and 130 aftershocks for the first 5 days. Dark-shaded and white areas indicate the zones of stress decrease and increase, respectively. The contour interval is 2 MPa. The star indicates the mainshock epicenter. Locations of the mainshock and all aftershocks have been determined by RESCO.

dynamic stress triggering aftershocks (e.g., Harris, 1998), provide similar estimates except near the fault edges because of the propagating rupture.

The mainshock of the 22 January 2003 earthquake (02h 06m 35sec) was followed by quite a large number of small to moderate ($M_w < 5.7$) aftershocks, but its major activity seems to have decayed in the first 2 weeks. The locations of these aftershocks have been determined from 10 stations of the Red Sismica de Universidad de Colima (RESCO). Figure 12 also shows the locations of 130 aftershocks for the first 5 days after the mainshock event, superposed on a map of the calculated stress change. It can be seen that there are three main clusters of aftershocks; one is trending in the north-northeast–south-southwest direction just northeast of the mainshock epicenter, the second one is located at the west side of the mainshock fault, and the third one is located on and just west of asperity B. The two largest aftershocks, M_w 5.7 (19h 41m, 22 January) and M_w 5.3 (20h 15m, 22 January), took place in the second cluster. More than 80% of aftershocks in the first cluster occurred in the zone of stress increase located southeast of asperity B. Aftershocks in the second cluster appear to have taken place both in the zones of stress increase and decrease, but the stress pattern northeast of this cluster is not reliable. On the other hand, aftershocks in the third cluster occurred on and west of the central part of stress drop zone. Also to be noted here is the lack of aftershock activity in and around a zone of large stress-drop, asperity A, although this might be due to some incapability of aftershock locations from the inland seismic stations. These patterns suggest that at least some of these aftershocks, in particular, in the first cluster, appear to have been triggered by a stress increase due to the nonuniform rupture process of the mainshock. However, the overall correlation between the aftershock location and the stress pattern is not clear, and later aftershock activity also expanded to the surrounding regions. This may be a common feature in previous studies in which some aftershocks can be related to stress triggers but some others occur in stress shadows (e.g., Harris, 1998).

Summary

We constructed a detailed source model of the 22 January 2003, Tecomán, Colima, Mexico earthquake, using the near-source records obtained by the UNAM plus the teleseismic data collected by IRIS-DMC. To construct the source model in an objective fashion, we developed a numerical method. We incorporated prior information into the observed data and determined the optimal relative weights of information from the observed data and prior constraints us-

ing an optimized ABIC. We found that the rupture process can be divided into three stages: the rupture nucleated near the hypocenter (stage I), then it broke the first asperity centering at about 15 km southwest from the epicenter (stage II); and the rupture propagated to the northeast and large asperity was broken (stage III). The somewhat longer rise time on the first shallower asperity than on the second, deeper one might be explained by variable frictional properties of the plate interface. The rupture area appears to extend parallel to the transition zone between the RIVE and COCOS plates. The hypocenter is located near a narrow part of the slip area, where the amount of slip is very small. It appears that at least one cluster of aftershocks for the first 5 days took place in and adjacent to the zones of stress increase because of the fault rupture during the mainshock.

Acknowledgments

The broadband and accelerogram data used in this study are from the Servicio Sismologico Nacional of Instituto de Geofisica and Instituto de Ingenieria of Universidad Nacional Autonoma de Mexico. We thank Dr. Shri Krishna Singh for making these data available for this study. The aftershock data were provided by the RESCO, Universidad de Colima, Mexico. We thank Dr. Yukitoshi Fukahata for his beneficial advice on ABIC formulation and Dr. David J. Wald, Dr. Chen Ji, and Dr. Jeanne Hardebeck for their critical reviews. This study was supported, in part, by the CONACyT (Mexico) Project 41209-F.

References

Akaike, H. (1980). Likelihood and Bayes procedure, in *Bayesian Statistics*, J. M. Bernardo, M. H. DeGroot, D. V. Lindley, and A. F. M. Smith (Editors), University Press, Valencia, Spain, 143–166.

Bandy, W., C. Mortera-Gutíerrez, J. Urrutia-Fucugaushi, and T. W. C. Hilde (1995). The subducted Rivera-Cocos plate boundary: Where is it, what is it, and what is its relationship to the Colima rift? *Geophys. Res. Lett.* **22**, 3075–3078.

Bilek, S. L., and T. Lay (2002). Tsunami earthquakes possibly wide spread manifestations of frictional conditional stability, *Geophys. Res. Lett.* **29**, doi 10.1029/2002GL015543.

Centroid Moment Tensor (CMT) Catalog, www.seismology.harvard.edu/CMTsearch.html (last accessed 1 May 2003).

DeMets, C., and S. Stein (1990). Present-day kinematics of the Rivera plate and implications for tectonics of southwestern Mexico, *J. Geophys. Res.* **95**, 21,931–21,948.

DeMets, C., and D. S. Wilson (1996). Relative motions of the Pacific, Rivera, North American, and Cocos plates since 0.78 Ma, *J. Geophys. Res.* **102**, 2789–2806.

Fukahata, Y., Y. Yagi, and M. Matsu'ura (2003). Waveform inversion for seismic source processes using ABIC with two sorts of prior constraints: comparison between proper and improper formulations, *Geophys. Res. Lett.* **30**, doi 10.1029/2002GL016293.

Fukahata, Y., A. Nishitani, and M. Matsu'ura (2004). Geodetic data inversion using ABIC to estimate slip history during one earthquake cycle with viscoelastic slip-response functions, *Geophys. J. Int.* **156**, 140–153.

Harris, R. A. (1998). Introduction to special issue: stress triggers, stress shadows, and Implications for seismic hazard, *J. Geophys. Res.* **103**, 24,347–24,358.

Hartzell, S. H., and T. H. Heaton (1983). Inversion of strong ground motion and teleseismic waveform data for the fault rupture history of the 1979 Imperial Valley, California earthquake, *Bull. Seism. Soc. Am.* **73**, 1553–1583.

Jackson, D. D., and M. Matsu'ura (1985). A Baysian approach to nonlinear inversion, *J. Geophys. Res.* **90**, 581–591.

Kikuchi, M., and H. Kanamori (1991). Inversion of complex body wave-III, *Bull. Seism. Soc. Am.* **81**, 2335–2350.

Kohketsu, K. (1985). The extended reflectivity method for synthetic near-field seismograms, *J. Phys. Earth* **33**, 121–131.

Lawson, C. L., and R. J. Hanson (1974). *Solving Least Squares Problems*, Prentice-Hall, Englewood Cliffs., New Jersey.

Mikumo, T., and T. Miyatake (1993). Dynamic rupture processes on a dipping fault, and estimates of stress drop and strength excess from the results of waveform inversion, *Geophys. J. Int.* **112**, 481–496.

Mikumo, T., Y. Yagi, S. K. Singh, and M. A. Santoyo (2002). Coseismic and postseismic stress changes in a subducting plate: possible stress interactions between large interplat thrust and intraplate normal-faulting earthquakes, *J. Geophys. Res.* **107**, no. B1, 10, ESE 5-1–5-12.

Okada, A. (1992). Internal deformation due to shear and tensile faults in a half-space, *Bull. Seism. Soc. Am.* **82**, 1018–1040.

Pacheco, J., S. K. Singh, J. Domínguez, A. Hurtado, L. Quintanar, Z. Jiménez, J. Yamamoto, C. Gutiérrez, M. Santoyo, W. Bandy, M. Guzmán, V. Kostoglodov, G. Reyes., and C. Ramírez (1997). The October 9, 1995 Colima-Jalisco, Mexico earthquake (M_w 8): an aftershock study and a comparison of this earthquake with those of 1932, *Geophys. Res. Lett.* **24**, 2223–2226.

Pardo, M., and G. Suárz (1995). Steep subduction geometry of the Rivera plate beneath the Jalisco block in western Mexico, *Geophys. Res. Lett.* **20**, 2391–2394.

Singh, S. K., J. F. Pacheco, L. Alcántara, G. Reyes, M. Ordaz, A. Iglesias, S. M. Alcocer, C. Gutierrez, C. Valdés, V. Kostoglodov, C. Reyes, T. Mikumo, R. Quaas, and J. G. Anderson (2003). A Preliminary Report on the Tecomán, Mexico Earthquake of 22 January 2003 (M_w 7.4), *Seism. Res. Lett.* **74**, 279–289.

Yoshida, S. (1992). Waveform inversion for rupture process using a non-flat seafloor model: application to 1986 Andreanof Islands and 1985 Chile earthquake, *Tectonophysics* **211**, 45–59.

Appendix

In this appendix, we have tried to check the effects of (1) the assumed structure, (2) the assumed depth of the hypocenter, (3) the assumed dip of the fault plane, and (4) the assumed location of the hypocenter by using synthetic tests. The synthetic data corresponding to the actual station distribution is exactly the same as in the synthetic test in the Source Rupture Process.

At first, we calculated the Green's function with a simple structure model that is given in Table A1 and inverted the source model for three different data sets: both of the teleseismic body-wave and near-source data; only the teleseismic body waves; and only the near-source data. The source models obtained from each data set are shown in Figure A1. From this figure, we can see that the slip patterns inverted from each data set can be reproduced. The slip distribution inverted only from the teleseismic body-wave data seems to maintain its stability, whereas the slip distribution inverted only from the near-source data tends to be concentrated into small patches. This suggests that only the result from the near-source data is sensitive with the assumed structure. To obtain the stable solution, it is important to use the teleseismic body-wave data.

Next, we calculated the Green's function with two slightly different depths of hypocenter, 17.5 and 22.5 km,

Table A1
Structure

V_p (km/sec)	V_s (km/sec)	Density (10^3 kg/m^3)	Q_p	Q_s	Thickness (km)
For teleseismic body wave					
1.5	0	1.0			1.0
5.69	3.29	2.70			8.0
6.27	3.62	2.80			9.7
6.71	3.87	2.90			17.3
8.10	4.68	3.30			—
For strong ground motion					
5.69	3.29	2.70	500	250	9.0
6.27	3.62	2.80	600	300	9.7
6.71	3.87	2.90	800	400	17.3
8.10	4.68	3.30	1200	600	—

and inverted the source model for three different data sets. The source models obtained from each data set are shown in Figure A2. The slip patterns inverted from each data set are reproduced. The slip distribution inverted only from the near-source data seems to be stable for the assumed depths. On the other hand, because the teleseismic body waves well constrain the depth range of the rupture area, the slip distributions inverted only from teleseismic body waves are sensitive with the assumed depths. To obtain a stable solution, it is important to obtain the depth of the hypocenter using teleseismic body waveforms.

Next, we calculated the Green's function with two slightly different dip angles, 20° and 23°, and inverted the source model for three different data sets. The source models obtained from each data set are shown in Figure A3. The slip patterns inverted from each data set seem to be well reproduced. The slip distribution inverted both from the teleseismic body-wave and near-source data is almost the same as the assumed slip distribution, whereas the slip models inverted only from the teleseismic body-wave or near-source data are sensitive with the dip angle.

Finally, we calculated the Green's function with two slightly different horizontal locations of the hypocenter located 5 km east and 5 km west from the true hypocenter and inverted the source model for three different data sets. The slip patterns inverted from each data set seem to be well reproduced.

International Institute of Seismology and Earthquake Engineering
Building Research Institute
1 Tatehara, Tsukuba, Ibaraki-ken
305-0802, Japan
yagi@kenken.go.jp
(Y.Y.)

Instituto de Geofisica
Universidad Nacional Autonoma de Mexico
Ciudad Universitaria, Mexico 04510 D.F., Mexico
(T.M., J.P.)

Resco, Universidad de Colima
Colima, Mexico
(G.R.)

Manuscript received 14 May 2003.

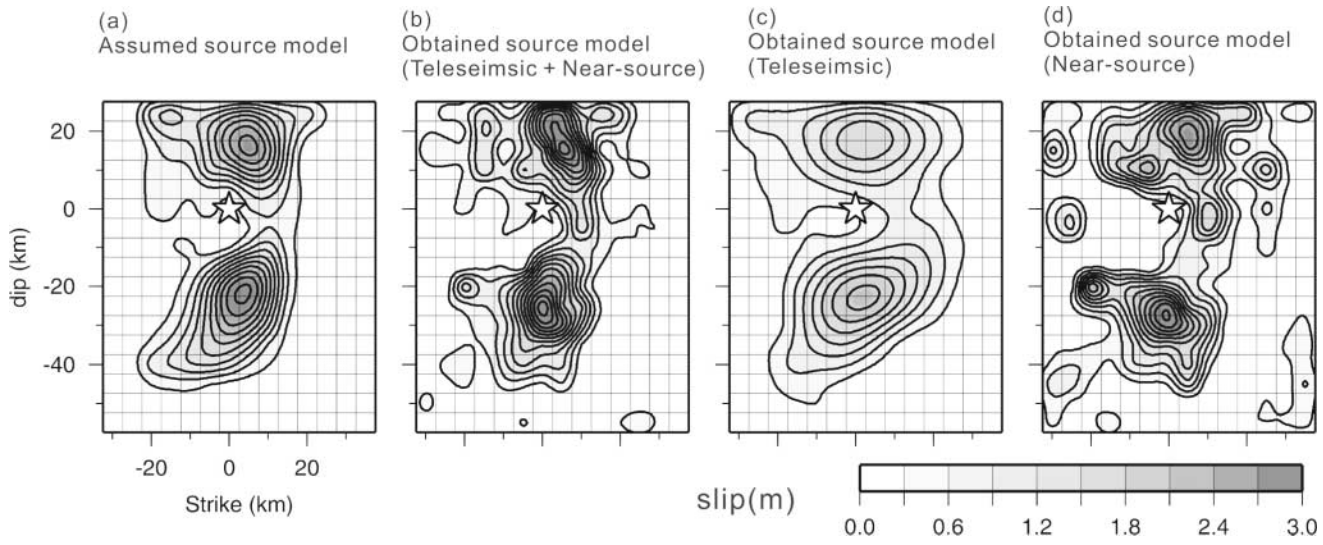

Figure A1. Results from a synthetic test with the wrong Green's function calculated with a simple-structure model given in Table A1. (a) Slip distribution of the assumed source model. (b) Slip distribution obtained from both the teleseismic body-wave and the near-source data. (c) Slip distribution obtained from the teleseismic body wave. (d) Slip distribution obtained from the near-source data.

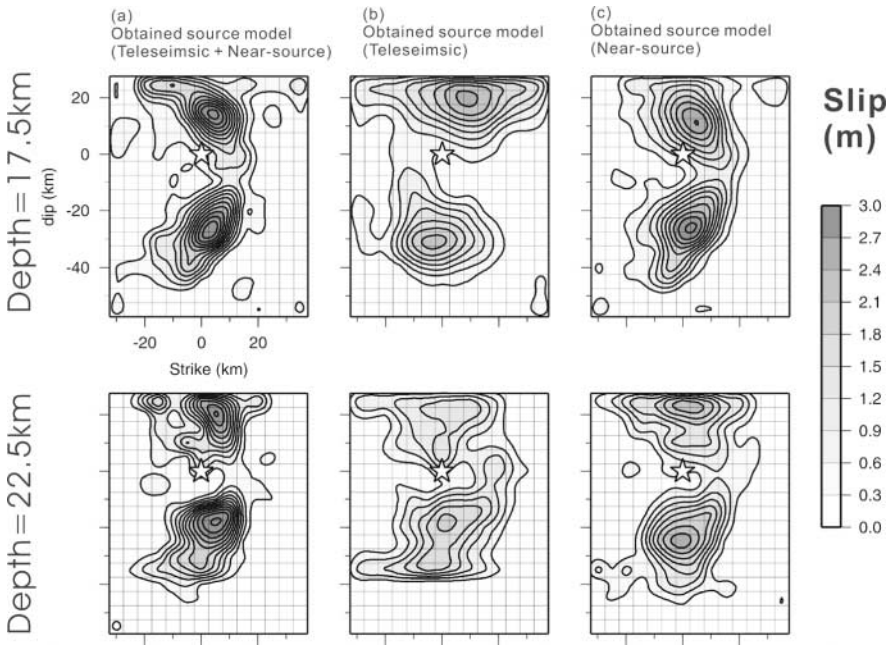

Figure A2. Results from a synthetic test with two slightly different depths of hypocenter. (a) Slip distribution obtained from both the teleseismic body-wave and the near-source data. (b) Slip distribution obtained from the teleseismic body waves. (c) Slip distribution obtained from the near-source data. (Top) Results for a depth of 17.5 km. (Bottom) Results for a depth of 22.5 km.

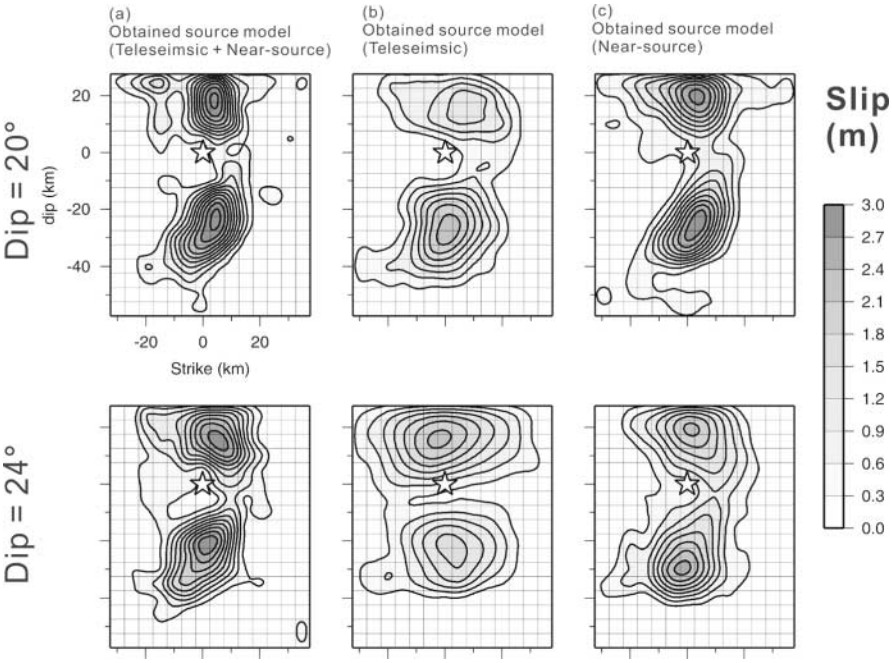

Figure A3. Results from a synthetic test with two slightly different dip angles. (a) Slip distribution obtained from both the teleseismic body-wave and near-source data. (b) Slip distribution obtained from the teleseismic body waves. (c) Slip distribution obtained from the near-source data. (Top) Results for a dip of 20°. (Bottom) Results for a dip of 24°.

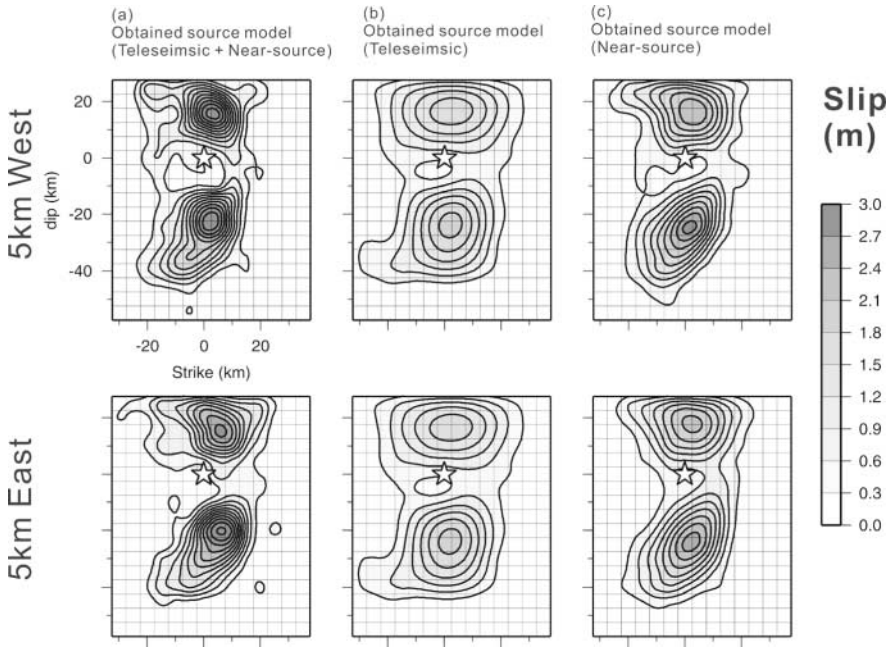

Figure A4. Results from a synthetic test with two slightly different horizontal locations of hypocenter. (a) Slip distribution obtained from both the teleseismic body-wave and near-source data. (b) Slip distribution obtained from the teleseismic body waves. (c) Slip distribution obtained from the near-source data. (Top) Results for the location 5 km west. (Bottom) Results for the location 5 km east from the true hypocenter.